

## RADIO POLARIZATION STUDY IN PROTOSTELLAR JETS

MARIANA CÉCERE<sup>1,5</sup>, PABLO F. VELÁZQUEZ<sup>2</sup>, ANABELLA T. ARAUDO<sup>3</sup>, FABIO DE COLLE<sup>2</sup>,  
 ALEJANDRO ESQUIVEL<sup>2</sup>, CARLOS CARRASCO-GONZÁLEZ<sup>4</sup>, AND LUIS F. RODRÍGUEZ<sup>4</sup>

*Draft version March 27, 2019*

### ABSTRACT

Synchrotron radiation is commonly observed associated with shocks of different velocities, ranging from relativistic shocks associated with, e.g., active galactic nuclei, gamma-ray bursts or microquasars to weakly- or non-relativistic flows as those observed e.g. in supernovae and supernova remnants. Recent observations of polarization in protostellar jets are important not only because they extend the range over which the acceleration process works, but also because they allow to measure directly the jet and interstellar magnetic field structure and intensity, thus giving insights on the jet ejection mechanism itself. In this paper, we compute for the first time polarized (synchrotron) and non polarized (thermal-X-ray) synthetic emission maps from axisymmetrical simulations of magnetized protostellar jets. We consider models with different jet velocities and variability, as well as toroidal or helical magnetic field. Our simulations show that variable, low-density jets with velocities  $\sim 1000$  km s $^{-1}$  and  $\sim 10$  times lighter than the environment can produce internal knots with significant synchrotron emission, and thermal X-rays in the shocked region of the leading bow shock moving in a dense medium.

*Subject headings:* Herbig-Haro objects, ISM: jets and outflows, magnetohydrodynamics (MHD), polarization, radiation mechanisms: non-thermal, shock waves

### 1. INTRODUCTION

Jets are present in astrophysical sources with various spatial scales, from Young Stellar Objects (YSOs) to active galactic nuclei. These collimated outflows are generally considered to be the result of bipolar ejection of plasma, associated with accretion onto a central object (Blandford & Payne 1982). Variability in the ejection speed can produce internal shocks clearly seen in YSO jets in the form of bright optical knots (e.g., Raga & Noriega-Crespo 1998; Masciadri et al. 2002) called Herbig-Haro (HH) objects.

Jets that arise from active galaxies can have relativistic speeds, and are well known synchrotron radiation emitters (see for example Tregillis et al. 2001; Laing et al. 2006; Gómez et al. 2008). In contrast, YSO jets are non-relativistic and thermal radio sources. However, a few stellar sources, such as Serpens (Rodríguez et al. 1989), HH 80-81 (Marti et al. 1995), Cepheus-A (Garay et al. 1996), W3 (Girart et al. 2002), and IRAS 16547-4247 (Garay et al. 2003) present radio emission with negative spectral index interpreted as non-thermal (synchrotron) radiation. Notably, polarized radio emission was detected in the inner jet of HH 80-81 (Carrasco-González et al. 2010). Therefore, an interesting question to answer is how jets with velocities of  $\sim$  a several hundreds km s $^{-1}$  moving into a dense medium

are able to produce shocks where particles can be accelerated up to relativistic energies and produce synchrotron radio emission.

We present a polarization study in order to shed light on the understanding of the non-thermal emission in protostellar jets. We model, by using axisymmetric, magnetohydrodynamic (MHD) simulations, the synchrotron emission produced by particles accelerated by adiabatic shocks in protostellar jets, and we compute the resulting polarization map. The paper is organized as follows: in Section 2, we describe the model and the numerical setup; in Section 3 we show the results (synthetic radio and X-ray emission maps); and in Section 4 we present our conclusions.

### 2. NUMERICAL CALCULATIONS

#### 2.1. Initial setup

Our study is based on 2.5D axisymmetric, MHD simulations carried out with the adaptive mesh refinement, eulerian code *Mezcal* (De Colle & Raga 2006; De Colle et al. 2008, 2012). We consider a 2D axisymmetrical adaptive grid, with a size of 0.2 and 0.5 pc along the  $r$ - and  $z$ -directions, respectively, and a maximum spatial resolution of  $1.56 \times 10^{-4}$  pc, corresponding to  $1280 \times 3200$  cells (at the maximum resolution) along the  $r$ - and  $z$ -directions, and 6 levels of refinement. The environment in which the jet propagates is homogeneous, with a uniform density  $n_{\text{env}} = 3000$  cm $^{-3}$ , temperature  $T_{\text{env}} = 100$  K, and magnetic field  $B_0$ . The jet is imposed at every time-step in a region of the computational domain with  $r < R_{\text{jet}} = 0.03$  pc and  $z < 0.003$  pc, with density  $n_{\text{jet}} = 260$  cm $^{-3}$  and velocity  $v_{\text{jet}}$  (along the  $z$ -axis). The longitudinal magnetic field (imposed on all computational domain) is  $B_z = B_0$ , and the toroidal

<sup>1</sup> Instituto de Astronomía Teórica y Experimental, Universidad Nacional de Córdoba, X5000BGR, Córdoba, Argentina

<sup>2</sup> Instituto de Ciencias Nucleares, Universidad Nacional Autónoma de México, Apdo. Postal 70-543, CP: 04510, D.F., México

<sup>3</sup> University of Oxford, Astrophysics, Keble Road, Oxford OX1 3RH, UK

<sup>4</sup> Centro de Radioastronomía y Astrofísica, Universidad Nacional Autónoma de México, Apdo. Postal 3-72, 58090, Morelia, Michoacán, México

<sup>5</sup> Consejo Nacional de Investigaciones Científicas y Técnicas (CONICET), Argentina.

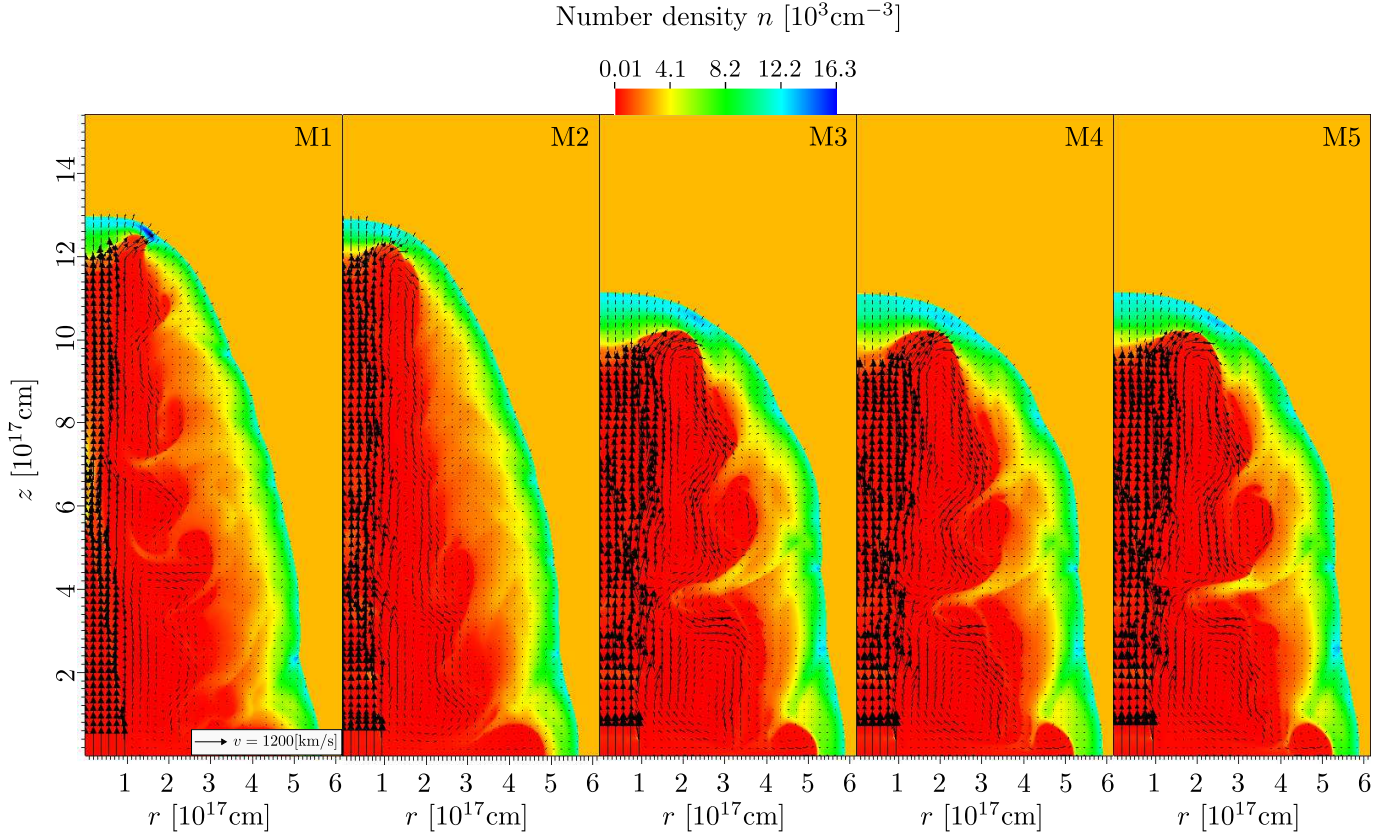


FIG. 1.— Number density stratification maps, in units of  $10^3 \text{ cm}^{-3}$ , and displayed in linear color scale. The integration time is  $t = 1500$  yr, in all models. The black arrows depict the velocity field (in units of  $\text{km s}^{-1}$ ).

component is given by (Lind et al. 1989)

$$B_\phi(r) = \begin{cases} B_m \left( \frac{r}{R_m} \right) & 0 \leq r < R_m; \\ B_m \left( \frac{R_m}{r} \right) & R_m \leq r < R_{\text{jet}}; \\ 0 & r \geq R_{\text{jet}}, \end{cases} \quad (1)$$

where  $R_m = 0.02$  pc, and  $B_m$  is given in the Table 1. The jet pressure profile is constructed to ensure total pressure equilibrium at  $t = 0$ :

$$p(r) = \begin{cases} \frac{B_m^2}{8\pi} \left( \beta_m - \frac{r^2}{R_m^2} \right) & 0 \leq r < R_m; \\ \frac{B_m^2}{8\pi} \left( \beta_m - \frac{R_m^2}{r^2} \right) & R_m \leq r < R_{\text{jet}}; \\ p_{\text{env}} & r \geq R_{\text{jet}}, \end{cases} \quad (2)$$

where  $\beta_m = p_{\text{env}}/(B_m^2/8\pi)$  and  $p_{\text{env}} = n_{\text{env}} k_B T_{\text{env}}$ .

We consider five different initial configurations. Model M1 represents a continuous jet with constant injection velocity  $v_{\text{jet}} = v_0$ , whereas models M2, M3, M4 and M5 have a time dependent injection velocity of the form

$$v_{\text{jet}} = v_0(1 + \Delta v \cos(\omega t)), \quad (3)$$

where  $v_0 = 1000 \text{ km s}^{-1}$  is the mean velocity of the flow, and  $\omega = 2\pi/\tau$ ,  $\tau = 50$  yr and  $\Delta v$  are the frequency, periodicity, and amplitude of the variability, respectively. The values of  $\Delta v$ ,  $B_z$  and jet maximum velocity  $v_{\text{max}} = v_0(1 + \Delta v)$  for the different models are given in Table 1.

## 2.2. Synthetic emission maps

### 2.2.1. Non-thermal radio emission and Stokes parameters

TABLE 1  
INITIAL SETUP

Model	$B_z$ [mG]	$B_m$ [mG]	$\Delta v$	$v_{\text{max}}$ [km s $^{-1}$ ]
M1	0	0.1	0	1000
M2	0	0.1	0.2	1200
M3	0	0.1	0.4	1400
M4	$0.1/\sqrt{2}$	$0.1/\sqrt{2}$	0.4	1400
M5	$0.1/\sqrt{10}$	$0.3/\sqrt{10}$	0.4	1400

Synchrotron emission in YSO jets is produced by relativistic electrons accelerated in shocks. In YSO jets, these can be originated by a supersonic variability in the injection velocity of the material (see equation 3), forming the so-called “internal shocks”, or by the deceleration of the jet by its interaction with the external surrounding medium. In the present study, we consider that a small fraction of the jet plasma is accelerated and injected in the shock downstream region with a power-law energy distribution  $N_e = KE_e^{-p}$ , where  $p = 2\alpha + 1 = 2$  for the standard spectral index  $\alpha = 0.5$  and  $K \propto \epsilon v_s^{-b}$ , being  $v_s$  the shock velocity. As in Orlando et al. (2007), the exponent  $b$  was chosen to be  $-1.5$ , implying that stronger shocks are more efficient accelerating particles. The synchrotron specific intensity is obtained as (Ginzburg & Syrovatskii 1965)

$$i(\nu) \propto KB_{\perp}^{\alpha+1} \nu^{-\alpha}, \quad (4)$$

where  $B_{\perp}$  is the component of the magnetic field perpendicular to the line of sight (LoS) and  $\nu = 5$  Ghz is the frequency. In this study, a dependence with the angle between the shock normal and the post-shocked mag-

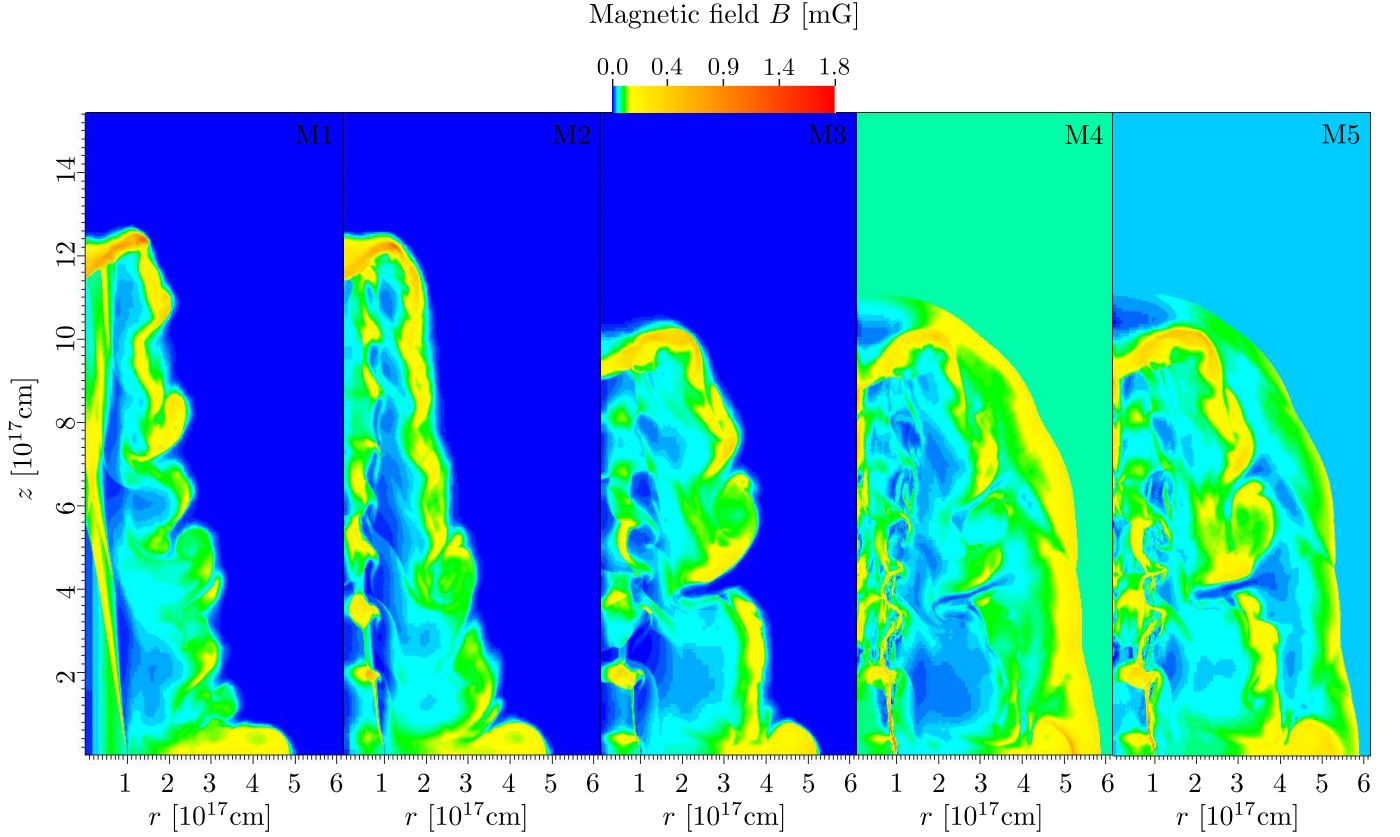


FIG. 2.— Maps of the total magnetic field intensity, (in units of mG) obtained for all models at an integration time of 1500 yr.

netic field is not considered, i.e. the acceleration mechanism is the isotropic (see for instance [Orlando et al. 2007](#); [Petruk et al. 2009](#); [Schneiter et al. 2015](#) for a discussion of the acceleration mechanisms in supernova remnants).

We compute the Stokes parameters  $Q_B$  and  $U_B$  as

$$Q_B(\nu) = \int_{LoS} f_0 i(\nu) \cos [2\phi(s)] ds, \quad (5)$$

$$U_B(\nu) = \int_{LoS} f_0 i(\nu) \sin [2\phi(s)] ds, \quad (6)$$

(see e.g. [Clarke et al. 1989](#); [Jun & Norman 1996](#)), where  $ds$  is measured along the LoS,  $\phi(s)$  is the position angle of the local magnetic field on the plane of the sky, and

$$f_0 = \frac{\alpha + 1}{\alpha + 5/3} \quad (7)$$

is the degree of linear polarization.

The linearly polarized intensity is given by

$$I_P(\nu) = \sqrt{Q_B^2(\nu) + U_B^2(\nu)} \quad (8)$$

and the position angle of the magnetic field, averaged along the LoS, is computed as

$$\chi_B = \frac{1}{2} \tan^{-1}(U_B/Q_B). \quad (9)$$

The polarization angle, i.e. the position angle with respect to the electric field  $\mathbf{E}$ , is obtained by replacing  $\phi(s) \rightarrow \phi(s) - \pi/2$  in Eqs. (5) and (6), that is magnetic field direction was rotated clockwise by

90° ([Schneiter et al. 2015](#)). Given that this study is not applied to any particular source, we neglect the Faraday rotation.

### 2.2.2. Thermal X-ray emission

We calculated the thermal emission by integrating the free-free emissivity  $j_\nu(n_e, T)$  along the LoS. In the low density regime,  $j_\nu(n_e, T) = n_e^2 \phi(T)$ , where  $n_e$  is the electron density and  $T$  is the temperature. We assume that the post-shock medium is fully ionized, i.e.  $n_e \sim n_H$ , where  $n_H$  is the ion density. The function  $\phi(T)$  was constructed with the CHIANTI atomic data base ([Dere et al. 1998](#)) considering the energy range [0.15-8] keV and assuming solar metallicity.

## 3. RESULTS

The numerical simulations with the initial conditions summarized in Table 1 were carried out until an integration time of 1500 yr.

### 3.1. Shocks in protostellar jets

As the jet interacts with the interstellar medium, it forms a double shock structure (the “working surface”), where the environment gas is accelerated by a forward shock, and the plasma injected at the base of the jet is decelerated by a reverse shock. This structure, as well as the contact discontinuity separating the shocked interstellar material from the shocked jet material, is clearly visible at the head of the jet shown in Figure 1.

Figure 1 displays in color scale the number density stratification and the velocity field. In the four cases,

a slow bowshock travels against the surrounding environment with velocities  $\sim 200 - 260 \text{ km s}^{-1}$ . Internal shocks are present only in the models where  $\Delta v \neq 0$  with velocities  $\sim 1000 - 1200 \text{ km s}^{-1}$ . With these velocities and considering that these shocks move in a low density medium (with densities of the order of  $10^{-1} \text{ cm}^{-3}$ ), the internal shocks are expected to be adiabatic. Note that in models M3, M4, and M5 ( $\Delta v = 0.4$ ) the bow shock is significantly slower than in models M1 and M2.

Figure 2 shows the magnitude of the magnetic field  $B$ . In models M2 and M3 the jet variability is quite evident by the presence of a thin Mach disk in several internal working surfaces. In contrast, the map corresponding to model M4 and M5 have a more complex morphology with less well defined internal working surfaces, and a larger cocoon structure due to the magnetic field along the symmetry axis.

### 3.2. Radio polarization study

We computed synthetic maps of linearly polarized intensity and thermal X-ray emission, and also maps of the distribution of polarization and position angle of  $B$ , as is shown in Figure 3. These maps were constructed considering that the jet axis is tilted  $15^\circ$  with respect to the plane of the sky. In this way, all models have magnetic field oriented both parallel or perpendicular to the symmetry axis (observations of  $B$  show such possible orientation). Note that, if we do not introduce an angle between the symmetry axis and the plane of the sky, for models M1-M3 we only obtain magnetic field perpendicular to the symmetry axis.

The lack of velocity variability in M1 model implies that the jet develops a single radio knot, while in the variable jet models several knots are obtained. Most of the radio emission of these knots is associated with the jet material and internal shocks or working surfaces and not with the main bow shock. When the magnetic field has a longitudinal component, the emission originates not only from internal shocks, but also from the head of the bow shock. This fact is clearly observed in the  $I_P$  map corresponding to model M4 (which has the larger value for  $B_z$ ). This is an important result since it would allow to discriminate whether the synchrotron emission in YSO jets is due to the jet magnetic field or the field in the interstellar medium. At the same time the X-ray emission also show knots but it occurs mainly in the bow shock, as suggested by Bonito et al. (2004, 2007, 2010) in hydrodynamic simulations.

## 4. DISCUSSION AND CONCLUSIONS

Carrasco-González et al. (2010) have shown the existence of polarized non-thermal emission associated with the HH 80-81 protostellar jet. However, this issue has not been studied by HD or MHD simulations. We present the results obtained from 2.5 MHD simulations of an adiabatic and low-density YSO jet. We have considered the cases of a jet with a constant or a time-dependent velocity ejection. Furthermore, cases in which the magnetic field is toroidal or which also has a  $z-$  component were

analyzed.

In order to carry out a qualitative comparison with observations, synthetic non-thermal (radio) and thermal (X-rays) emission maps were calculated from our numerical results. The greatest difference between the two type of emissions is that in all models without or small longitudinal magnetic field, the thermal emission arises mainly from the environmental material shocked by the main bow shock, while non-thermal emission is associated with internal shocks or working surfaces. This result is in agreement with that reported by the hydrodynamic simulations presented by Bonito et al. (2004, 2007, 2010).] The distribution of both thermal and non-thermal emissions are similar to each other for model M4, which correspond to the case with the longest value of  $B_0$ .

Radio maps show two main results. Firstly, the variability in jet velocity is important in generating bright knots of synchrotron emission, which are produced when slow jet material is caught up by faster jet material. And secondly, the non-thermal radio emission comes mostly from the internal shocks (which have velocities of the order of  $1000 \text{ km s}^{-1}$ ), suggesting that this emission is due to the intrinsic magnetic field associated with the jet material. This can be understood by noting that in this work we are considering a jet with a fixed axis, and thus the working surfaces move along the axis of symmetry of the jet and never exit the cocoon carved by the main bow shock. Thus, their interaction is with the jet material and not with the external medium.

Also, we have analyzed the distribution of the polarization and the position angle of the magnetic field, which clearly display magnetic field parallel or perpendicular to the symmetry axis for model M4 and M5, while models M1-M3 mainly display magnetic field perpendicular to this axis.

In this paper, assuming that relativistic electrons are produced efficiently in adiabatic stellar jets, we have used standard prescriptions to compute the synchrotron emission produced by the accelerated electrons. Our results show that while the thermal X-ray emission is dominated by the shocked environment material located at the head of the jet. At the same time a jet with a time-dependent ejection velocity and a magnetic field associated with it can produce several radio knots. We have also shown that the synchrotron radiation intensity and the polarization angle depend strongly on the magnetic field orientation and intensity. A detailed comparison with the results of the HH 80-81 jet can then potentially be used to infer the magnetic field associated with protostellar jets.

Authors thank financial support from CONACyT grants 167611 and 167625, CONICET-CONACyT grant CAR 190489, and DGAPA-PAPIIT (UNAM) grants IG100214, IA103115, IA109715, IA103315. We also thank Enrique Palacios for maintaining the Linux Server on which the simulations were carried out.

## REFERENCES

Blandford, R. D., & Payne, D. G. 1982, MNRAS, 199, 883

Bonito, R., Orlando, S., Miceli, M., Eislöffel, J., Peres, G., & Favata, F. 2010, A&A, 517, A68

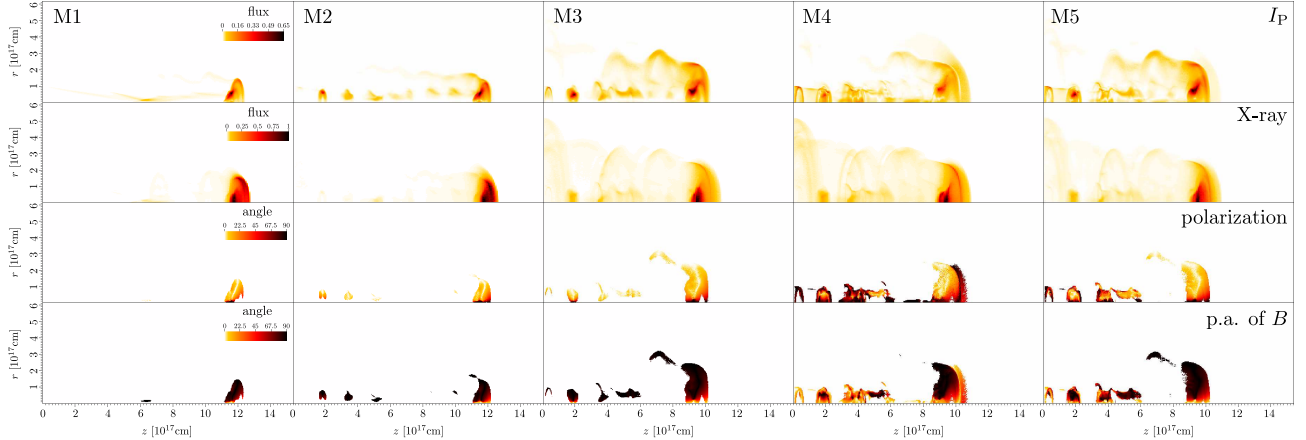


FIG. 3.— Top to bottom: synthetic maps of the linearly polarized intensity, X-ray flux, polarization and position angle of  $B$ . Left to right: M1-M5 models. These maps were performed considering that the jet axis is tilted  $15^\circ$  with respect to the plane of the sky.

Bonito, R., Orlando, S., Peres, G., Favata, F., & Rosner, R. 2004, *A&A*, 424, L1  
—. 2007, *A&A*, 462, 645

Carrasco-González, C., Rodríguez, L. F., Anglada, G., Martí, J., Torrelles, J. M., & Osorio, M. 2010, *Science*, 330, 1209

Clarke, D. A., Burns, J. O., & Norman, M. L. 1989, *ApJ*, 342, 700

De Colle, F., & Raga, A. C. 2006, *A&A*, 449, 1061

De Colle, F., Raga, A. C., & Esquivel, A. 2008, *ApJ*, 689, 302

De Colle, F., Ramirez-Ruiz, E., Granot, J., & Lopez-Camara, D. 2012, *ApJ*, 751, 57

Dere, K. P., Landi, E., Mason, H. E., Fossi, B. C. M., & Young, P. R. 1998, in *Astronomical Society of the Pacific Conference Series*, Vol. 143, The Scientific Impact of the Goddard High Resolution Spectrograph, ed. J. C. Brandt, T. B. Ake, & C. C. Petersen, 390

Garay, G., Brooks, K. J., Mardones, D., & Norris, R. P. 2003, *ApJ*, 587, 739

Garay, G., Ramirez, S., Rodriguez, L. F., Curiel, S., & Torrelles, J. M. 1996, *ApJ*, 459, 193

Ginzburg, V. L., & Syrovatskii, S. I. 1965, *ARA&A*, 3, 297

Girart, J. M., Curiel, S., Rodríguez, L. F., & Cantó, J. 2002, *RMAA*, 38, 169

Gómez, J. L., Marscher, A. P., Jorstad, S. G., Agudo, I., & Roca-Sogorb, M. 2008, *ApJ*, 681, L69

Jun, B.-I., & Norman, M. L. 1996, *ApJ*, 472, 245

Laing, R. A., Canvin, J. R., Bridle, A. H., & Hardcastle, M. J. 2006, *MNRAS*, 372, 510

Lind, K. R., Payne, D. G., Meier, D. L., & Blandford, R. D. 1989, *ApJ*, 344, 89

Marti, J., Rodriguez, L. F., & Reipurth, B. 1995, *ApJ*, 449, 184

Masciadri, E., Velázquez, P. F., Raga, A. C., Cantó, J., & Noriega-Crespo, A. 2002, *ApJ*, 573, 260

Orlando, S., Bocchino, F., Reale, F., Peres, G., & Petruk, O. 2007, *A&A*, 470, 927

Petruk, O., Dubner, G., Castelletti, G., Bocchino, F., Iakubovskyi, D., Kirsch, M. G. F., Miceli, M., Orlando, S., & Telezhinsky, I. 2009, *MNRAS*, 393, 1034

Raga, A., & Noriega-Crespo, A. 1998, *AJ*, 116, 2943

Rodriguez, L. F., Curiel, S., Moran, J. M., Mirabel, I. F., Roth, M., & Garay, G. 1989, *ApJ*, 346, L85

Schneiter, E. M., Velázquez, P. F., Reynoso, E. M., Esquivel, A., & De Colle, F. 2015, *MNRAS*, 449, 88

Tregillis, I. L., Jones, T. W., & Ryu, D. 2001, *ApJ*, 557, 475